Supporting Information for "Seismic attenuation and S-velocity structures in D″ beneath Central America using 1-D full-waveform inversion"

Anselme F.E. Borgeaud[1], Frédéric Deschamps[1]

[1]Institute of Earth Sciences, Academia Sinica, Taipei, Taiwan

Contents of this file

Corresponding author: A. F. E. Borgeaud, Institute of Earth Sciences, Academia Sinica, No. 128, Section 2, Academia Road, Nangang District, 115 Taipei City, Taiwan (anselme@earth.sinica.edu.tw)

Corresponding author: Frédéric Deschamps, Institute of Earth Sciences, Academia Sinica, No. 128, Section 2, Academia Road, Nangang District, 115 Taipei City, Taiwan (frederic@earth.sinica.edu.tw)

8. Figure S4. Synthetic test without iterative inversion

9. Figure S5. L-curves

10. Figure S6. Misfit distributions

11. Figure S7. Misfit improvement as function of the epicentral distance

12. Figures S8. Record section of stacked waveforms

13. Table S1. Events used in this study

14. Table S2. Re-determined source time functions used in this study

15. Table S3. List of the IRIS DMC seismic network codes used in this study

Text S1. Focusing of S waves due to Farallon slab

ScS/S amplitude ratios are commonly used to study the Q_S structure of the lowermost mantle (Fisher et al., 2003; Ford et al., 2012; Durand et al., 2013; Konishi et al., 2020). As for the ScS-S differential travel time, the ScS/S amplitude ratio reduces the effect of the 3-D structure near the source and receiver. However, it also includes the effects of the 3-D structure near the turning point of the S phase.

In the explored region, S-waves sample a complex 3-D structure due to the presence of the subducted Farallon slab near their turning depths (between 1825–2245 km depth), which causes large variations in the amplitude of observed S-waves (Fig. S1). Fig. S1a, plotting the S-wave amplitude ratio (data/PREM synthetics) for event cluster S and waveforms filtered between 12.5–200 s, shows that S-waves amplitudes increase in corridor S2, and decrease in corridors S3 and S4. This pattern of anomalies can (partially) be explained using synthetics for SEMUCB_WM1, computed using SPECFEM3D for one event in cluster S (event #19 in Table S1) (Fig. S1b). Since they cannot be reproduced by synthetics for SEMUCB_WM1 truncated at depth 1000 km (i.e., excluding the structure near the S-wave turning points) (Fig. S1c), these amplitude variations are most likely due to the structure near the S-waves turning points, and not near the receiver or the source. The amplification of S-waves in corridor S2 is due to the presence of a low-velocity trough at their turning points (see Fig S1d), between the Farallon slab to the east, and another high-velocity structure to the west.

The large lateral variations in S-wave amplitude in the data make it difficult to use the S-wave as a reference phase to correct ScS amplitudes. We therefore decided not to use it, except for an average amplitude correction in the re-determination of source time

functions. We note that localized small-scale anomalies in the upper mantle affect ScS waveforms and amplitudes in a way that is not corrected for in this study. However, previous studies using a dataset similar to ours have presented various tests showing that such upper mantle anomalies do not affect the inferred V_S structure in the lowermost mantle (e.g., Figs. S3 and S4 in Borgeaud et al., 2017). This is due to the use of a large number of waveforms sampling nearly the same region in the lowermost mantle, but different regions in the upper mantle, which makes the partial derivative kernel for the lowermost mantle nearly independent (orthogonal) from that for the upper mantle. Similarly, (Figs. S5 and S6 in Konishi et al., 2020) have shown that the inferred V_S and Q_S structures of the lowermost mantle are nearly unchanged, whether or not the rest of the mantle is included in the inversion. Although (Konishi et al., 2020) use a different dataset than ours, they also use the ScS phase with an epicentral distance range similar to ours, and a slightly smaller number of waveforms than in this study, so that their results should also be applicable to our study.

Text S2. Re-determination of source time functions

In order to reduce errors on waveform amplitudes due to the source parameters, we re-infer source time functions and moment magnitudes (the other source parameters, i.e. moment tensor and centroid time and location, being fixed to those given in the GCMT catalog). Re-determination of source time functions and moment magnitudes is important for several reasons. First, amplitude information is the main constraint to infer Q_S. Furthermore, we use relatively high-frequency waveforms (five events in our dataset have GCMT durations larger than the minimum period used in this study). Finally, the GCMT

catalog possibly over-estimates the duration of source time functions for intermediate and deep earthquakes (Yamaya et al., 2018).

To re-determine the source time functions, we compute green functions for each events (using the GCMT catalog for the centroid and moment tensor) with the DSM (Kawai et al., 2006) and perform a grid search. The parameters for the grid search are the duration of triangle source time functions (from 1 to 20 s, by 0.25 s increments), and an amplitude correction (from 0.5 to 2 times, by 0.05 increments). We then choose the parameters that minimize the following misfit in a time window around the S phase:

$$\phi_{\text{stf}} = \sum_n \left[0.5 \left(1 - \frac{\mathbf{u}_n \cdot \mathbf{s}_n}{|\mathbf{u}_n||\mathbf{s}_n|} \right) + \left| \ln \frac{\max(\mathbf{u}_n) - \min(\mathbf{u}_n)}{3\left(\max(\mathbf{s}_n) - \min(\mathbf{s}_n)\right)} \right| \right], \tag{1}$$

where $\mathbf{u}_n$, and $\mathbf{s}_n$ are the observed data, and synthetics for time window n, respectively. The scaling factor $\frac{1}{3}$ for the amplitude ratio is chosen so that records with amplitudes ratio smaller than 0.33 or larger than 3 have a misfit of 1.

The green functions and data are filtered between 6 and 200 s. This implies that durations significantly smaller than 6 s cannot be constrained, and results in several redetermined durations of 1 s (the minimum duration in our grid search). This is not a problem in this study, since only large durations have an effect on the synthetics. After redetermination, source time function durations range from 1 s to 6 s, and the amplitude corrections from 0.69 to 2. Re-determined durations are all smaller than that for the GCMT catalog, which is consistent with (Yamaya et al., 2018). Our catalog of source time functions is given in table S2.

Text S3. Choice of β and normalization of regularization matrices

The regularization matrices $\mathbf{\Gamma}$ and $\mathbf{\Lambda}$ in eq. (11) (main text) are normalized in order to have values comparable to the sensitivity kernel $\mathbf{A}^T\mathbf{W}_A\mathbf{A} + \beta\mathbf{B}^T\mathbf{W}_B\mathbf{B}$. To do so, we multiply the regularization matrices by $\left\|\mathbf{A}^T\mathbf{W}_A\mathbf{A}\right\|_\infty + \beta\left\|\mathbf{B}^T\mathbf{W}_B\mathbf{B}\right\|_\infty$, where $\|\cdot\|_\infty$ is the L_{inf} norm.

The parameter β in eq. 4 (main text) controls the relative importance of the waveform (ϕ_A) and spectral amplitude (ϕ_B) misfits. The limit cases $\beta = 0$, and $\beta \to \infty$ correspond to solutions constrained only by the waveform misfit, and spectral amplitude misfit, respectively. Since the spectral amplitude misfit is primarily used to better constrain the Q_S structure, we set $\beta = 0$ for all but the final iteration. For the final iteration, we set $\beta = \phi_A(m^{\text{final}-1})/\phi_B(m^{\text{final}-1})$. This gives the waveform and spectral amplitude misfits roughly the same importance in the inversion (for the final iteration).

Text S4. Validation of amplitude corrections for focusing due to lateral velocity variations

As mentioned in the main text, we use a single amplitude correction for all the waveforms in a given corridor. These corrections are averages over epicentral distances, and are computed for synthetics with a minimum period of 12.5 s. We show below that these simplifications are reasonable.

Fig. S2 shows the dependence on frequency of the ScS amplitude ratios used to compute the corrections, and is discussed in the main text. Fig. S3 shows the result of a synthetic test performed in order to verify the validity of the amplitude corrections used in this study. For this test, we use as input data the synthetics computed with SPECFEM3D for the 3D model in Fig. 3f, which sample the low-velocity corridor S3. Note that only V_S

is perturbed, while Q_S is not perturbed. We then perform two inversions (using PREM as the initial model), with and without applying amplitude corrections. The inversion without amplitude correction results in a generally well recovered V_S, while the average Q_S over the depth of our modelled region is 364.6, higher than PREM Q_S by 52.6. On the other hand, when amplitude corrections are used, the inverted average Q_S is 308.3, only slightly lower than PREM Q_S. From this test, we conclude that 1) amplitude focusing due to the presence of lateral velocity anomalies results in an artificially high inverted Q_S when not corrected for, and 2) the approximate amplitude corrections used in this study perform reasonably well, even though the dependence on epicentral distance and frequency is ignored.

References

Borgeaud, A. F. E., Kawai, K., Konishi, K., & Geller, R. J. (2017). Imaging paleoslabs in the D″ layer beneath Central America and the Caribbean using seismic waveform inversion. *Science Advances*, *3*(11). doi: 10.1126/sciadv.1602700

Durand, S., Matas, J., Ford, S., Ricard, Y., Romanowicz, B. A., & Montagner, J. (2013). Insights from ScS – S measurements on deep mantle attenuation. *Earth and Planetary Science Letters*, *374*, 101–110. doi: 10.1016/j.epsl.2013.05.026

Ekström, G., Nettles, M., & Dziewonski, A. M. (2012). The global CMT project 2004 – 2010 : Centroid-moment tensors for 13,1017 earthquakes. *Physics of the Earth and Planetary Interiors*, *200–201*, 1–9. doi: 10.1016/j.pepi.2012.04.002

Fisher, J. L., Wysession, M. E., & Fischer, K. M. (2003). Small-scale lateral variations in D" attenuation and velocity structure. *Geophysical Research Letters*, *30*(8), 1–4. doi: 10.1029/2002GL016179

Ford, S. R., Garnero, E. J., & Thorne, M. S. (2012). Differential t* measurements via instantaneous frequency matching: Observations of lower mantle shear attenuation heterogeneity beneath western Central America. *Geophysical Journal International*, *189*(1), 513–523. doi: 10.1111/j.1365-246X.2011.05348.x

Kawai, K., Takeuchi, N., & Geller, R. J. (2006). Complete synthetic seismograms up to 2 Hz for transversely isotropic spherically symmetric media. *Geophysical Journal International*, *164*(2), 411–424. doi: 10.1111/j.1365-246X.2005.02829.x

Konishi, K., Fuji, N., & Deschamps, F. (2020). Three-dimensional elastic and anelastic structure of the lowermost mantle beneath the Western Pacific from finite-frequency tomography. *Journal of Geophysical Research: Solid Earth*, *125*(2). doi: 10.1029/2019JB018089

Yamaya, L., Borgeaud, A. F., Kawai, K., Geller, R. J., & Konishi, K. (2018). Effects of redetermination of source time functions on the 3-D velocity structure inferred by waveform inversion. *Physics of the Earth and Planetary Interiors*, *282*, 117–143. doi: 10.1016/j.pepi.2018.04.012

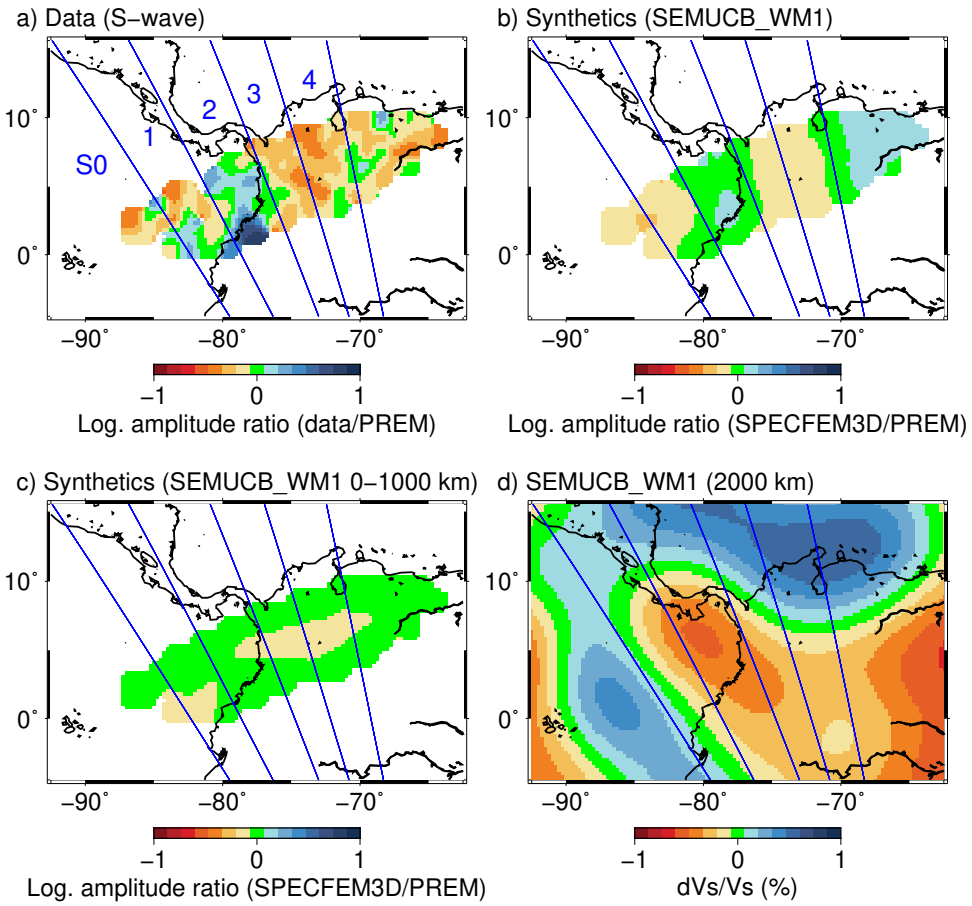

Figure S1. Effect of the mid-mantle Farallon slab on the S-wave amplitude ratio. Logarithm of the amplitude ratio between data and PREM for event cluster S (a), and specfem synthetics for SEMUCB-WM1 and PREM (b). (c) same as (b), but for SEMUCB-WM1 truncated at 1000 km in order to exclude the 3-D structure near the S-wave turning point. (d) Horizontal section through SEMUCB-WM1 at 2000 km depth. The blue lines labeled S0 to S4 (panel a) show the same corridors as in Fig. 1b.

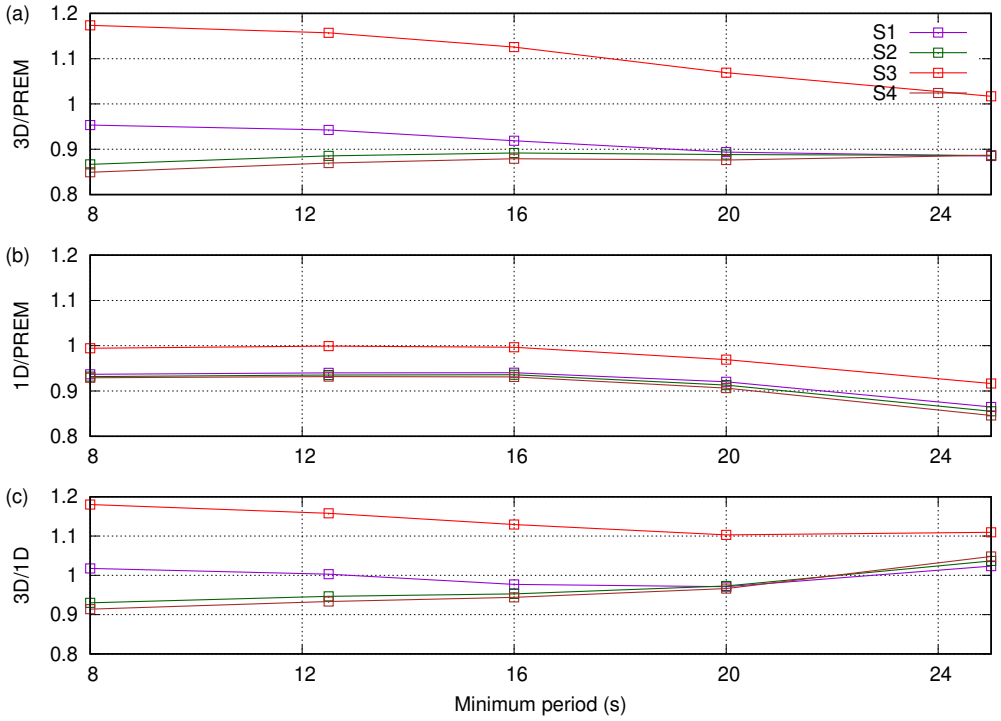

Figure S2. Frequency dependence of the amplitude ratios for the high-velocity corridors S1, S2, and S4, and the low-velocity corridor S3. The synthetics used to compute the amplitude ratios are filtered between the minimum period and 200 s. The panels show the amplitude ratios between a) SPECFEM3D and PREM synthetics, b) the 1-D inverted models and PREM synthetics, and c) the SPECFEM3D and 1-D inverted models synthetics. The ratios in panel (c) at 12.5 s are the ones used as amplitude corrections in the actual inversion.

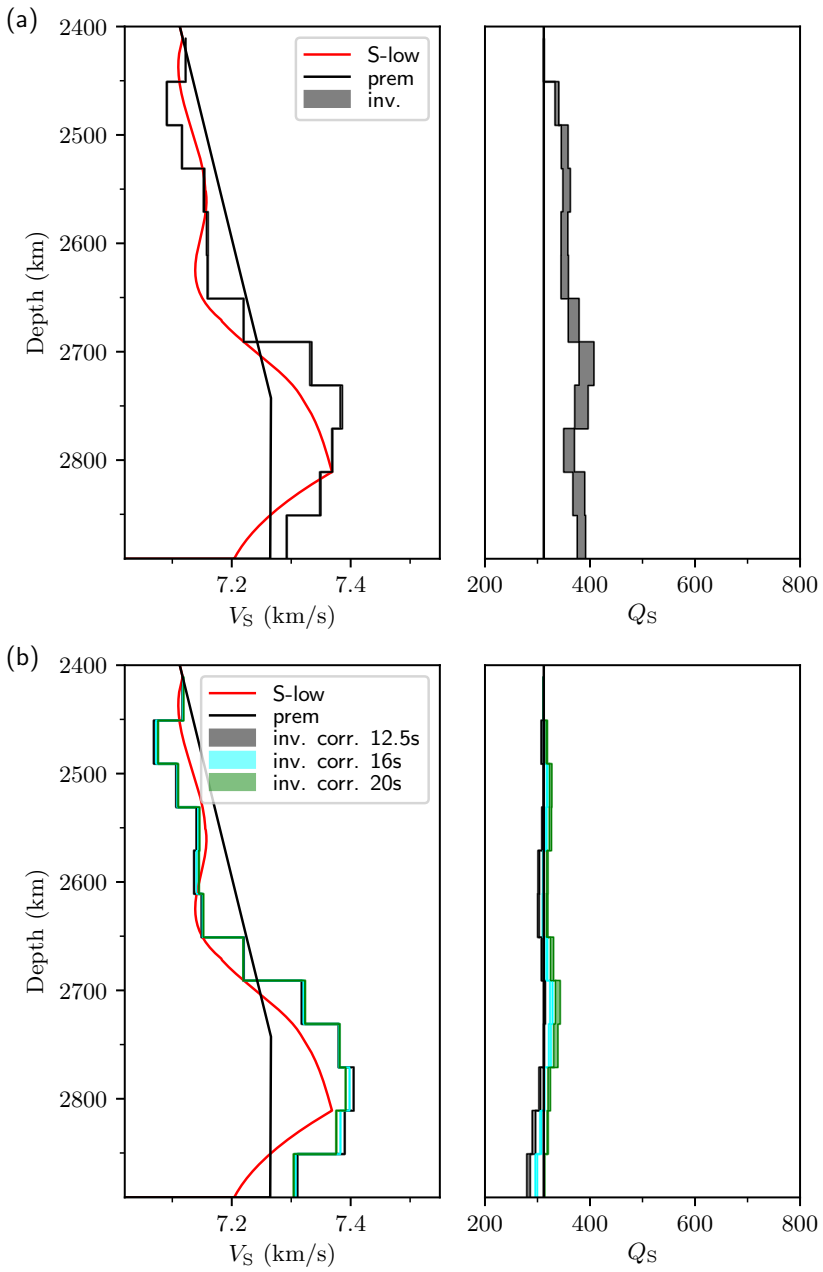

Figure S3. Synthetic test for validation of the amplitude corrections used in this study. The input synthetics are computed using SPECFEM3D for the model in Fig. 2f (i.e., the synthetics used to compute the amplitude corrections), and sampling the low-velocity corridor S3. The V_S model sampled by the input synthetics is labeled 'S-low' and shown in red. a) V_S and Q_S after inversion of the input synthetics without applying amplitude correction; b) Same as (a), but using amplitude corrections computed at 12.5 s, 16 s, and 20 s.

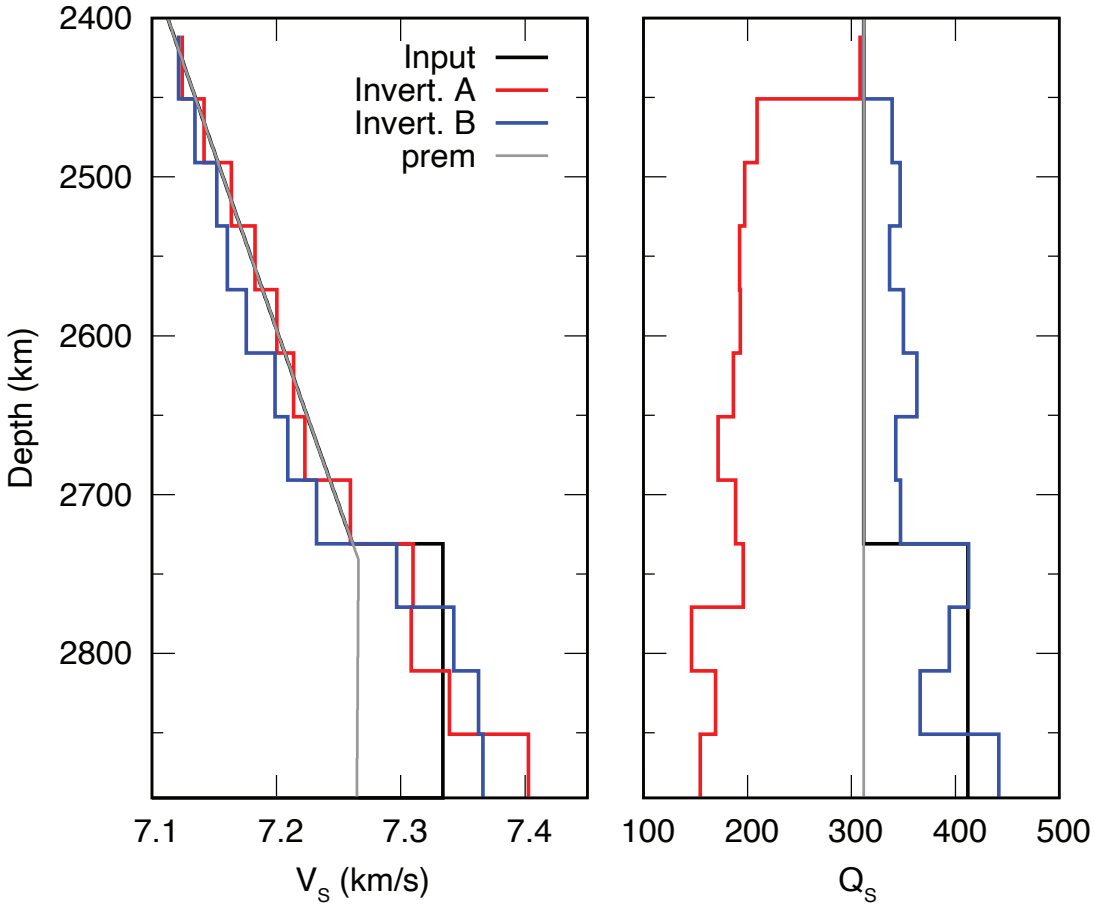

Figure S4. Synthetic test without iterative inversion. For this test, the input structure is the same as for Fig. 4c, but only one iteration for V_S and Q_S is performed (in contrast to Fig. 4c, showing models obtained after two iterations: V_S, and V_S+Q_S). The recovered Q_S structure shows that the spectral amplitude misfit (blue line; labeled B) is robust when the initial V_S structure is far from the actual V_S structure. By contrast, the Q_S structure inferred using the waveform misfit (red line; labeled A) is strongly contaminated by the trade-off with the V_S structure.

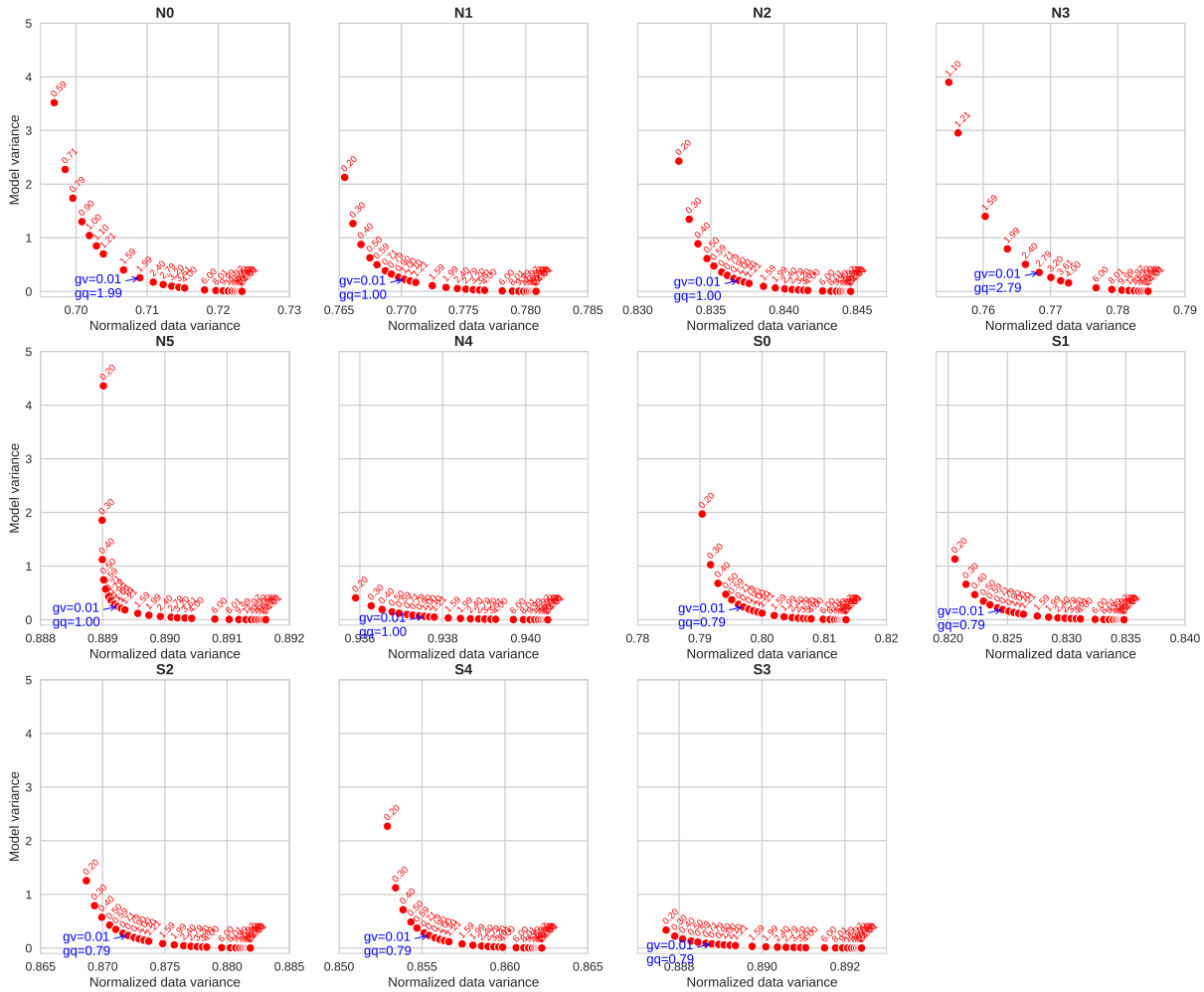

Figure S5. L-curves used to select the 'optimal' damping parameters for the Q_S structure (γ_q). The L-curves are obtained by varying γ_q from 0.2 to 24, with $\gamma_v = 0.01$, $\lambda_v = 0.01$, and $\lambda_q = 0.16$ kept constant (see main text). Each panel shows a separate corridor for clusters N and S. The 'optimal' γ_q is labeled in blue in each panel.

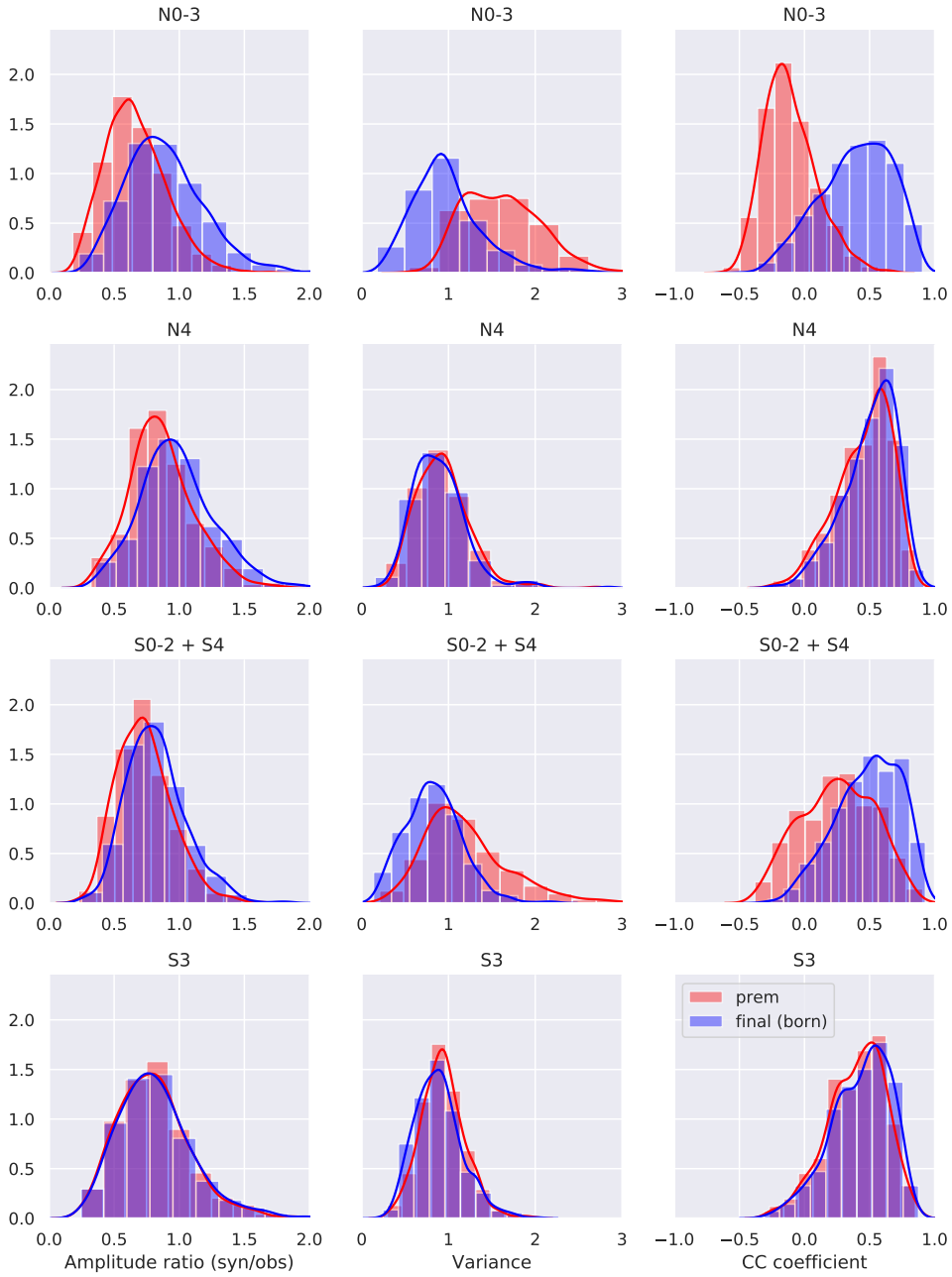

Figure S6. Distributions of amplitude ratios, variances, and cross-correlation coefficients for PREM (red) and our inverted models (blue) (Fig. 4 in the main text) for corridors N0 to N3 (top row), N4 (second row), S0 to S2 and S4 (third row), and S3 (bottom row).

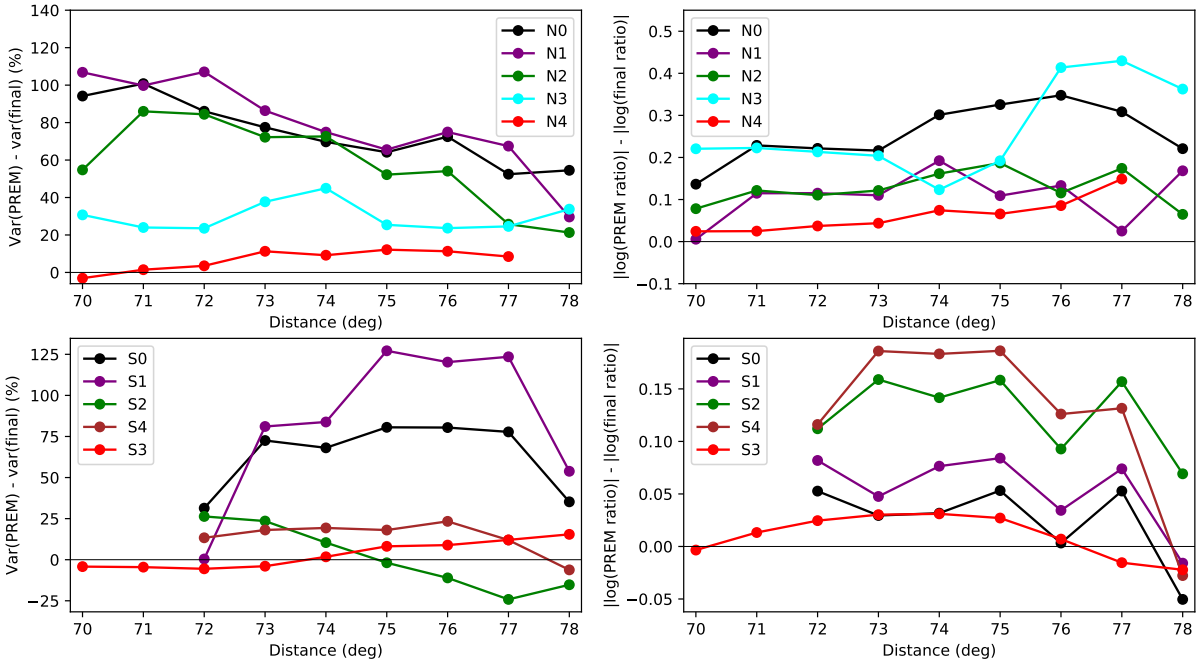

Figure S7. Improvement in waveform fit, and amplitude ratios as function of the epicentral distance for all corridors. *Left*: difference between the waveform misfit (eq. 1 in the main text) for PREM and for our inferred models, for the north (top) and south (bottom) corridors. *Right*: difference between the absolute value of the log of the amplitude ratios (synthetics over observed waveforms) for PREM and for our final models, for the north (top) and south (bottom) corridors. In all panels, positive y-axis values mean that our inferred models perform better than PREM, while negative values mean the opposite.

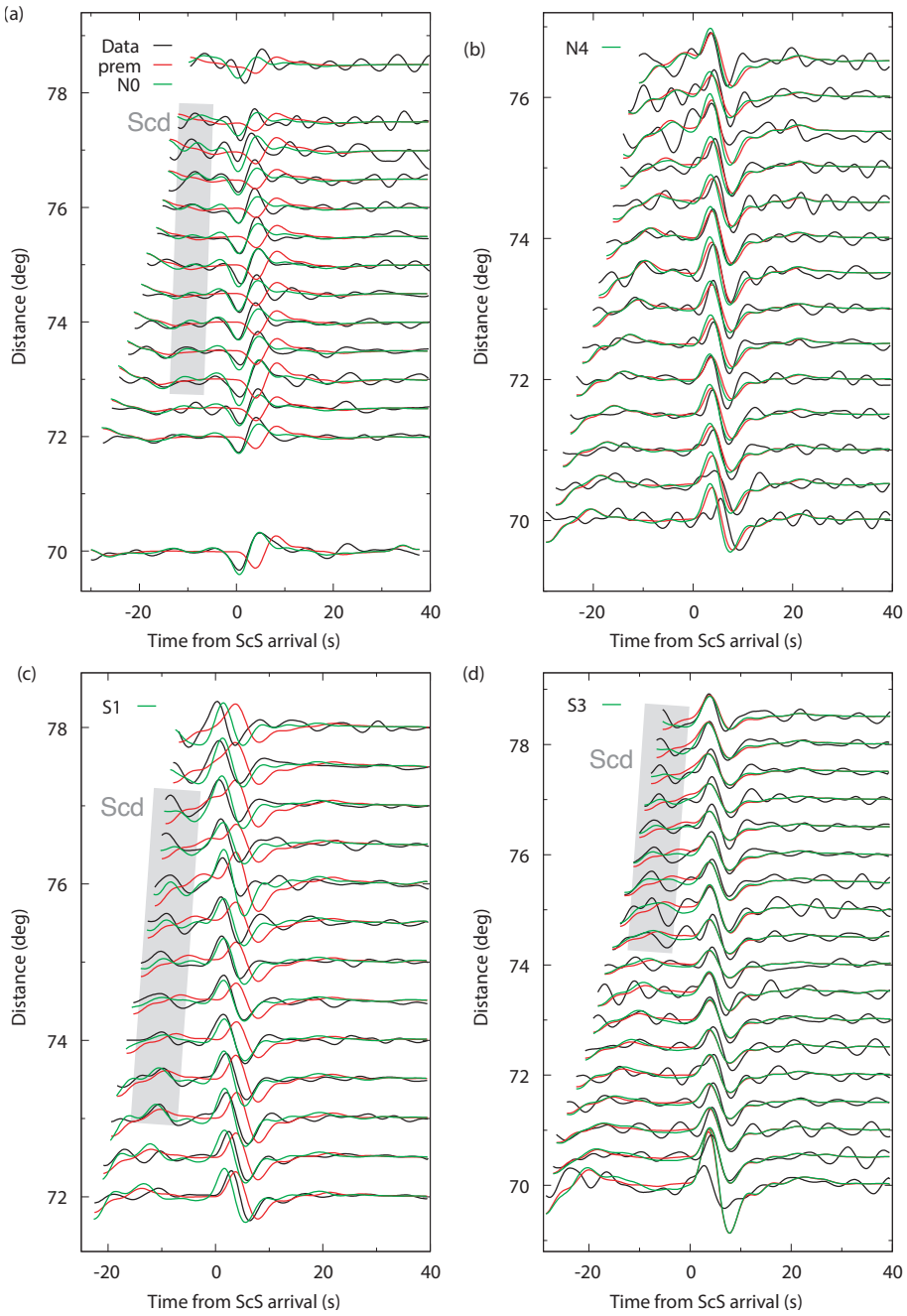

Figure S8. Record sections of stacked observed waveforms (black), and synthetics for PREM (red) and our inferred models (blue) (see Fig. 4 of the main text). a) event 12 sampling corridor N0, b) event 21 within 336-338° of azimuth sampling corridor N4, c) event 10 sampling corridor S1, d) event 23 within 338-340° of azimuth sampling corridor S3. The Scd phase, due to interaction with the D″ discontinuity, is highlighted in gray in panels a, c, and d.

#	Event ID	Latitude (deg)	Longitude (deg)	Depth (km)	Mw	Cluster
1	200503211223A	-24.9	-63.5	572.3	6.8	N
2	200503211243A	-24.7	-63.6	572.2	6.4	N
3	200510012154A	-23.6	-63.6	558.7	5.6	N
4	200609220232A	-26.8	-63.0	602.4	6.0	S
5	200610232100A	-21.8	-65.8	287.6	5.8	N
6	200611130126A	-26.1	-63.5	573.4	6.8	S
7	200704180108A	-24.2	-66.9	218.1	5.6	N
8	200707211534A	-22.3	-66.0	280.2	6.4	N
9	200711180540A	-22.7	-66.5	262.4	6.0	N
10	200809031125A	-26.8	-63.3	571.3	6.3	S
11	200810122055A	-20.3	-65.2	361.5	6.2	N
12	200911141944A	-23.0	-66.8	221.2	6.2	N
13	201001280804A	-23.6	-67.0	204.5	5.9	N
14	201002071709A	-23.4	-66.6	230.9	5.6	N
15	201007261731A	-24.3	-67.3	202.2	5.5	N
16	201104170158A	-27.6	-63.1	573.9	5.8	S
17	201109021347A	-28.6	-63.1	597.3	6.7	S
18	201203050746A	-28.2	-63.3	565.1	6.1	S
19*	201205280507A	-28.2	-63.1	591.6	6.7	S
20	201205281150A	-28.1	-63.1	595.2	5.5	S
21	201206020752A	-22.1	-63.6	549.5	6.0	N
22	201211221307A	-22.9	-63.7	544.4	5.9	N
23	201302221201A	-27.9	-63.0	585.7	6.1	S
24	201306081225A	-22.6	-66.9	215.3	5.6	N
25	201307022004A	-24.0	-66.7	225.8	5.7	N
26	201404180746A	-27.9	-62.6	629.3	5.6	S
27	201405140338A	-22.8	-66.6	239.0	5.6	N
28	201409241116A	-23.8	-66.7	227.6	6.2	N
29	201501171841A	-22.1	-63.2	572.6	5.5	N
30	201502111301A	-23.5	-66.8	219.5	5.5	N
31	201502111857A	-23.1	-66.8	223.0	6.7	N
32	201509281528A	-23.8	-66.9	221.4	6.0	N

Table S1. Events used in this study. Event #19 was not used in the final inversion for Q_S, because of the anomalously high amplitudes of ScS and Scd phases.

#	Event ID	Duration (gcmt) (s)	Duration (s)	Amp. corr.	Misfit	Misfit (gcmt)
1	200503211223A	12.8	5.0	1.05	0.13	0.45
2	200503211243A	7.6	2.0	0.87	0.19	0.28
3	200510012154A	3.2	1.0	1.40	0.21	0.34
4	200609220232A	4.6	1.0	1.30	0.19	0.29
5	200610232100A	4.0	2.5	1.20	0.19	0.23
6	200611130126A	12.8	5.5	0.87	0.11	0.33
7	200704180108A	3.0	1.0	1.25	0.00	0.00
8	200707211534A	8.0	3.5	0.91	0.13	0.21
9	200711180540A	5.0	1.0	1.20	0.18	0.27
10	200809031125A	5.0	1.0	1.10	0.17	0.25
11	200810122055A	6.0	3.5	1.10	0.18	0.24
12	200911141944A	5.8	1.5	1.05	0.18	0.24
13	201001280804A	4.2	1.0	1.15	0.20	0.26
14	201002071709A	3.2	1.0	2.00	0.21	0.50
15	201007261731A	2.8	1.0	1.20	0.19	0.23
16	201104170158A	3.8	1.0	1.20	0.19	0.26
17	201109021347A	10.8	1.0	0.69	0.17	0.33
18	201203050746A	5.6	1.0	1.60	0.20	0.47
19	201205280507A	10.6	6.0	0.91	0.12	0.23
20	201205281150A	2.6	1.0	1.05	0.20	0.22
21	201206020752A	4.8	1.0	1.10	0.19	0.25
22	201211221307A	4.4	1.0	1.35	0.16	0.31
23	201302221201A	5.4	1.0	1.20	0.17	0.30
24	201306081225A	3.2	1.0	1.25	0.19	0.25
25	201307022004A	3.4	1.0	1.45	0.21	0.32
26	201404180746A	3.0	1.0	1.20	0.19	0.25
27	201405140338A	3.2	1.0	1.20	0.18	0.23
28	201409241116A	6.4	1.0	1.20	0.17	0.36
29	201501171841A	2.8	1.0	1.90	0.23	0.46
30	201502111301A	2.8	2.8	1.80	0.21	0.36
31	201502111857A	10.8	3.5	1.10	0.14	0.42
32	201509281528A	4.8	1.0	1.20	0.14	0.24

Table S2. Re-determined source time functions used in this study. The last two columns, labeled 'Misfit' and 'Misfit (gcmt)', give the value of the misfit (eq. S1) when using the re-determined source time functions, and those from the GCMT catalog (Ekström et al., 2012), respectively.

Network code
7A
7C
AZ
BK
CI
CN
II
IM
IU
LB
LD
NN
TA
UO
US
UU
XA
XD
XE
XI
XN
XO
XQ
XR
XT
XU
XV
YH
YW
YX
Z9
ZG

Table S3. List of the IRIS DMC seismic network codes used in this study.